The Journal of the Astronautical Sciences
https://doi.org/10.1007/s40295-022-00348-6

ORIGINAL ARTICLE

Image Processing Robustness Assessment of Small-Body Shapes

Carmine Buonagura[1] · **Mattia Pugliatti**[1] · **Francesco Topputo**[1]

Accepted: 3 October 2022

Abstract

Asteroids and comets are triggering interest due to the richness of precious materials, their scientific value as well as for their potential hazardousness. Owing to their significant diversity, minor bodies do not exhibit uniform shapes: they can range from spherical to irregularly shaped objects with rocky, uneven, and cratered surface. Nowadays, space probes rely more and more on optical navigation techniques, due to the increasing demand for autonomy. When dealing with minor bodies, the diversified range of shapes can significantly affect the performance of these techniques. In order to enable deep space probes to confidently deal with uncertainties, the need for robust image processing methods arises. Commonly, few image processing methods are designed and tested with limited shapes to meet mission requirements. In this work, we depart from this paradigm by developing a new framework, which includes extensive testing of the image processing algorithms with various shapes. The shapes are not randomly analyzed, yet they are arranged in a hierarchical structure called hyper-cube. The cube allows for a better understanding of the methods performance and to infer the way they shift from one shape to the other. The novelty of this approach lies both in the cube representation, which allows a better understanding of the link between the image processing algorithms and shape of the object, but also in the extensive number of shapes that have been tested, which has never been done before. In this analysis, four methods are considered, namely: center of brightness, intensity weighted centroiding, correlation with Lambertian spheres, and least-squares-based ellipse fitting. Results from this test allow us correlating the methods performances to the bodies shape, to suggest the best performing method for each shape family, and to assess their robustness.

Keywords Image processing · Asteroids · Optical navigation · Small-body shape

✉ Carmine Buonagura
carmine.buonagura@polimi.it

[1] Department of Aerospace Science and Technology, Politecnico di Milano, Via La Masa 34, 20156 Milan, Italy

Published online: 07 November 2022

1 Introduction

Minor bodies exploration is becoming of growing interest due to resource exploitation, scientific interest, and planetary defence reasons [1]. Firstly, they contain an abundance of valuable resources that can either be mined or used to refuel spacecraft and overcome the technological limits of deep space exploration [2]. Secondly, they can help to investigate the planets accretion process and the solar system evolution [3]. Lastly, we need to characterize near-Earth asteroids, posing a constant threat for the Earth (up until 2019, the NEOWISE space telescope estimated $\sim 4700 \pm 1500$ Potentially Hazardous Asteroids (PHAs) larger than 140 m [4]).

Small bodies show a variety of shapes. Indeed, they span from spherical with no significant topological features to flat, bilobed, elongated and hemispherical ones [5]. The overall shape of about 3000 minor bodies is roughly estimated thanks to ground-based radar and light curve analysis, but it is precisely known for an handful amount of bodies through insitu observations.

Small-body rendezvous and fly-by missions demand a flight dynamic team on-ground that study in detail the spacecraft trajectory accordingly to the analyzed body. These calculations require that the shape of the body is accurately known in order to properly select the best suited Image Processing (IP) technique to optically navigate it. This information is not always available from on-ground observations, especially for interplanetary missions [6]. Due to the wide variety of shapes these bodies can assume, it is mandatory that the spacecraft is able to return good navigation results whatever the shape is.

Optical Navigation (OpNav) refers to the set of techniques that are used to get an estimate of the spacecraft state from images. In this field, there is an increasing need for autonomy [7]. For small-body close proximity operations, autonomy can be enabled exploiting images, as they can be easily available on-board spacecraft. The state estimation strongly depends on the IP method used to extract navigation observables from images [8]. These techniques provide information on the line-of-sight, but some of them can also return relative range estimations. The spacecraft state with respect to the minor body can be thus extracted exploiting filtering techniques.

The context of this work is the resolved regime, when the body's shape is clearly visible in the camera view, as opposite to the unresolved and surface feature ones where the body occupies just few pixels or fills the entire FOV, so that the information on the shape cannot be extracted. Current Image Processing algorithms are designed to work on spherical or ellipsoidal bodies [9–12] thus the need to test their robustness on different body's shapes. The most important methods in the considered regime are Center of Brightness (CoB), Intensity Weighted Centroiding (IWC), Centroid Apparent Diameter (CAD), Correlation with Lambertian Spheres (CLS) and Centerfinding by Correlation (CbC).

Artificial Intelligence (AI) techniques can also be exploited to provide IP solutions or position estimates [13–16] completely bypassing traditional approaches. In doing so, however, they rely on large amount of data for training and they lack full explainability when compared to traditional methods. These could be discouraging factors when facing undefined shapes and consequently lack of data.

For this reason, due to their simplicity and adaptability, only traditional methods will be analyzed in this work. CoB and IWC are the simplest to implement [17] and they are used in the unresolved regime as well. CAD methods exploit conics such as circle and ellipse to be fit with the detected limb of the small-body [10, 11, 18] while CLS and CbC techniques correlate the image with a template image of a Lambertian sphere [19, 20] and of the 3D model of the body at hand [8] respectively. From CAD, CLS and CbC methods it is possible to obtain an estimation of the overall size, and thus of the range. Only CLS and CbC directly take into account the lighting conditions. For the analysis in this work, CbC is discarded as it requires the knowledge of body shape, which is considered unknown. Moreover, least squares based Ellipse Fitting (EF) is considered as CAD technique. Even though other implementations are expected to be more accurate with tri-axial ellipsoid regular shapes [21, 22], the method considered in this work is the simplest to implement and can be considered as a good representative of all ellipse fitting methods. These four image processing methods (CoB, IWC, CLS, EF) are tested on synthetic images of artificially generated objects. The images are generated starting from the three-dimensional model of the known bodies, refining them introducing surface roughness, craters, boulders, and environmental conditions.

Existing work in literature has provided a comparison of image processing techniques for close proximity operations, but no work has been performed this analysis with a large number of small-body shapes and with a set of IP methods. Most relevantly, [8] performs comparison of IP methods for two different shapes while [23] assesses the performances of two IP techniques on planets. In short, these comparison are made with a limited variety of small-body's shapes or with a limited set of IP methods.

This work, differently from the previously mentioned ones, aims to assess the robustness of a set of traditional image processing algorithms in front of a wide variety of minor body shapes. The analysis is performed in an innovative way, arranging the bodies in a shape hierarchical structure, named shape-cube. The cube is designed to contain representative minor body shapes and to take care, at the time being, of the existing extreme cases in terms of elongation and irregularity. The selected real bodies are the starting point for the construction of the hyper-cube, as they are linearly interpolated between them to realize a progressive transition from one shape to another, and thus, better understand how the performance of the algorithms shifts as they move in the space of the cube. The novelty of this approach is twofold. In the first place, the cube allows for a better visualization and understanding of the relation between IP algorithm and minor body shape. An intuitive representation of the algorithms performance shift can be visualized as it has never been done before. In addition, this is the first time that a set of algorithms are tested on an extensive number of shapes. Thereby, the robustness of such algorithms can be reliably assessed.

As a result, the selected algorithms are tested on a large amount of minor body's shapes to determine their performance and robustness, and to understand what trends the error follows for each method based on the shape. This result can be exploited by the mission designer to choose the best technique accordingly to the body at hand. It is also possible to integrate this shape map on-board the spacecraft

in order to let it autonomously select the best performing method once information on the shape are available.

The paper is structured as follows. Section 2 reports a brief explanation of the considered IP techniques, with focus on the construction of the shape-cube and the generation of the synthetic images. In Sect. 3, the performances of each method on the analyzed shapes will be shown and the comparison among the different techniques will be made. Some considerations and future works are discussed in Sect. 4.

2 Methodology

The aim of this work is to evaluate the performances of the aforementioned image processing techniques in presence of a wide variety of shapes. It must be pointed out that these algorithms can be used on-board spacecraft to retrieve information about the center of mass and the range of the minor body from the acquired pictures for use by the filter.

To evaluate the robustness of these algorithms, 15 different minor body models are chosen[1,2] as the bases of a shape space. They span from near spherical to highly irregular shapes, they are arranged in a virtual cube, and they are the starting point for the generation of synthetic intermediate models whose characteristics embed the most significant features of the shapes they are generated from. In this way, it is possible to obtain a continuous transition from the shape of a model to another and visualize the error trend in the centroiding estimation. Each model is then visually improved introducing morphological features and placing it in a space environment with the aim of generate synthetic images on which the IP techniques are tested on.

2.1 Image Processing Algorithms

Center of brightness, intensity weighted centroiding, correlation with Lambertian spheres and ellipse fitting have been selected as representative methods of traditional IP methods. They are mature, well-known and robust methods already used in various missions. In this section the theory behind them will be briefly reviewed.

Center of Brightness This algorithm is the simplest to implement as it computes the barycenter of the pixel intensity of the image. The center of brightness algorithm accordingly to [24–26] is:

$$x_{cb} = \frac{\sum_{i=1}^{N}\sum_{j=1}^{N} I_{ij}x_{ij}}{\sum_{i=1}^{N}\sum_{j=1}^{N} I_{ij}}, \quad y_{cb} = \frac{\sum_{i=1}^{N}\sum_{j=1}^{N} I_{ij}y_{ij}}{\sum_{i=1}^{N}\sum_{j=1}^{N} I_{ij}} \tag{1}$$

where I_{ij} is the intensity of the generic pixel (i, j) whose coordinates are $(x_{i,j}, y_{i,j})$, and x_{cb} and y_{cb} are the Center of Brightness (CoB) coordinates.

[1] https://astro.troja.mff.cuni.cz/projects/damit/asteroids/browse, Last access: March 22, 2021.
[2] https://sbn.psi.edu/pds/shape-models/, Last access: March 22, 2021.

Unlike asteroids, comets' CoB are highly affected by outgassing. For instance, Halley's images showed multiple, large bright jets emanating from the comet and a dark nucleus barely visible [24]. The effect of these type of phenomena are not investigated in this work, which includes comets only for what concerns their characteristic shapes.

Intensity Weighted Centroiding In intensity weighted centroiding [27] the weighting function is the intensity distribution of the spot pattern I_{ij}. The center of brightness position is estimated as:

$$x_{cb} = \frac{\sum_{i=1}^{N}\sum_{j=1}^{N} I_{ij}^2 x_{ij}}{\sum_{i=1}^{N}\sum_{j=1}^{N} I_{ij}^2}, \quad y_{cb} = \frac{\sum_{i=1}^{N}\sum_{j=1}^{N} I_{ij}^2 y_{ij}}{\sum_{i=1}^{N}\sum_{j=1}^{N} I_{ij}^2} \tag{2}$$

This algorithm is exploited under low light level conditions and low background noise [27].

IWC and CoB are highly affected by the Sun phase angle resulting in an offset of the center of brightness from the Center of Mass (CoM). Scattering models can be used to correct for this shift. For regular bodies the most common ones are analytical corrections such as the Lambertian and Lommel–Seeliger [8], which are applicable both for spherical bodies but are also derived for ellipsoidal ones in [28]. On the other hand, data-driven methods could be best suited for highly irregular shapes, as it is illustrated in [29, 30]. These models are not taken into account in this work.

Correlation with Lambertian Spheres The CLS method exploits the spherical approximation of the minor body. A Lambertian sphere is an object that reflects light in all directions, regardless of the angle of incidence obeying Lambertian's cosine law. The basic idea of this method, used in the Hera mission [19], is to compare the image of the minor body with a template image of a Lambertian sphere. The templates are images generated in Matlab rendering a family of spheres with various radius while applying Lambert's cosine law. These are generated around an initial guess which is provided by the body radius in pixel R_{px}, computed as an approximation from the number of illuminated pixels n_{px} and the portion of the visible sphere δ as:

$$R_{px} = \sqrt{\frac{n_{px}}{\delta\pi}} \tag{3}$$

The normalized cross-correlation consists in placing a template image at all possible positions (x, y) of the input image f and measure the similarity between the template t and a window $W(x, y)$ out of f. It can be computed as:

$$\gamma(u,v) = \frac{\sum_{x,y}[f(x,y) - \bar{f}_{u,v}][t(x-u, y-v) - \bar{t}]}{\{\sum_{x,y}[f(x,y) - \bar{f}_{u,v}]^2 \sum_{x,y}[t(x-u, y-v) - \bar{t}]^2\}^{0.5}} \tag{4}$$

where $\bar{t}$ is the mean of the template, $\bar{f}_{u,v}$ is the mean of the image in the window $W(x, y)$ under the template, and (u, v) is the coordinate of a feature. The best matching Lambertian sphere is obtained and so the best estimate of the object centroid and range. In Fig. 1 the entire procedure from the synthetic image to the centroid

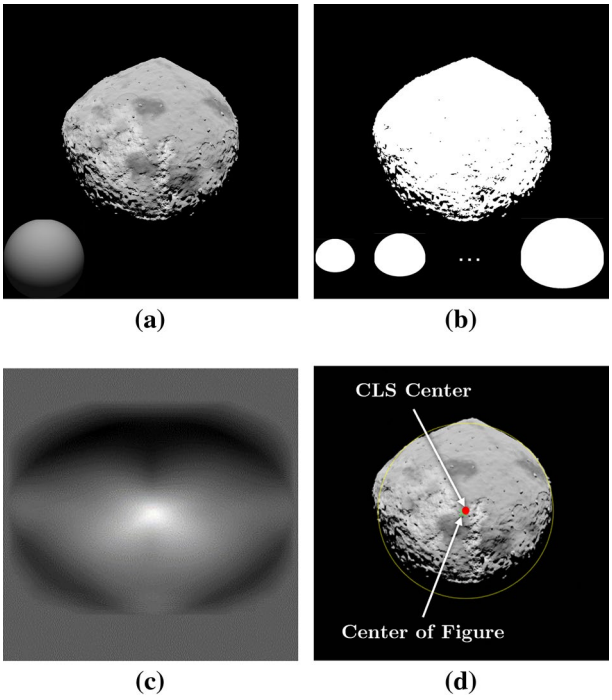

Fig. 1 Correlation with Lambertian spheres algorithm steps. **a** Generation of a Lambertian sphere characterized by the real lighting conditions represented as a template image on the bottom left. **b** Binarization of both images and comparison with different sphere sizes reported on the bottom. **c** Normalized cross-correlation result. **d** Final result with the estimated centroid's position depicted as a red dot and the real position as a green ×

estimation is depicted. The detailed algorithm steps are reported in [19] and [20]. It is important to state that in this work it is assumed that the Sun phase angle is always known for rendering the Lambertian sphere on-board.

Ellipse Fitting Ellipse fitting is a technique used when the target object can be approximated to an ellipsoid. This method exploits the object perspective projection onto the image plane. If the body is assumed to be a triaxial ellipsoid, then its projection is an ellipse. Thus, the final goal is to fit the boundary points of the minor body in the image with this conic. This approach is used in the LUMIO mission, but in that case, it only works for regularly shaped objects [9, 31]. Moreover, it must be taken into account that this method returns better results when wide portions of the minor body are visible. The summary of the algorithm steps are in Fig. 2.

The most important step is the fitting one as it must determine the model parameters that approximate the available data at best. The fitting reliability depends on its robustness to outliers and noise. Furthermore, an optimization method is required to overcome local minima and determine the most suitable parameters. One of the most commonly used techniques is the least squares method [32].

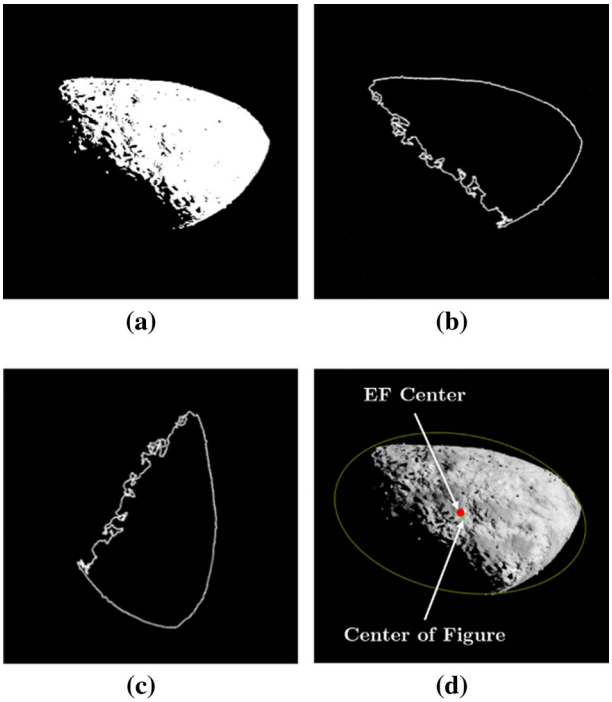

Fig. 2 Steps required for the ellipse fitting technique. **a** Conversion to binarized image. **b** Extraction of the boundary points. **c** Rotation of the points in order to have the light vector parallel to the vertical axis. **d** Fit of an ellipse to the boundary points and rotate them back. The estimated centroid's position is represented as a red dot, the real position as a green ×

Once the boundary points have been determined it is possible to fit them with an ellipse, with the objective to minimize the difference among the points of the curve and of the boundary E, namely

$$E = \sum_{j=1}^{N} ||\mathbf{b}(\theta_j) - \mathbf{e}(\theta_j)|| \tag{5}$$

where $\mathbf{b}$ are the coordinates of the boundary points in the image, $\mathbf{e}$ are the ones of the ellipse, θ is the angular coordinate and N is the number of boundary samples.

Methods Comparison The performances of the analyzed methods can be outlined highlighting how they behave at different distances and Sun phase angles. In general, Correlation with Lambertian spheres and ellipse fitting work better when the target object is clearly visible in the camera sensor while center of brightness and intensity weighted centroiding show their best in the unresolved regime, when the body spans only few pixels in the image. Clearly, the four methods return different outputs. CoB and IWC can only provide an information about the CoM position while CLS and EF can also return an estimation of the body radius, and thus it is possible to compute the range from it.

Table 1 Summary of the examined image processing techniques

Name	Regime	PROs	CONs	Output
CoB	Unres, Res	Easy to implement	Shape of the spot not considered	CoM
IWC	Unres, Res	Easy to implement	Low background noise required	CoM
CLS	Res	Considers lighting conditions	Spherical approximation	CoM, Radius
EF	Res	Flexible	Ellipsoidal approximation	CoM, Radius

Concerning the Sun phase angle all methods return the smallest errors when the body is clearly visible. Regarding the CoB and IWC the problem arise when the Sun phase angle is different from 0, as the CoB shifts toward the illuminated region of the minor body. In this situation the light scattering methods can be exploited in order to reduce the offset.

For what concerns the EF method it must be remarked that the fitting algorithm works well when the Sun phase angle is close to 0 deg, that is when the body is completely visible. However, for high phase angles it is unable to approximate the minor body shape as it does not take into account the terminator, and for this reason its performances deteriorate. Lastly, the CLS technique is not affected by the phase angle of the Sun, since it takes into account the lighting conditions.

A summary of the most important features of the examined methods is reported in Table 1. Resolved and unresolved regimes are abbreviated as “res” and “unres”, respectively.

2.2 Shape-Cube Construction

The shape-cube is a virtual cubic structure made of small bodies that are part of the shape space. First, shape bases are selected from already visited asteroids in order to test centroiding algorithms to existing shapes. Thereby, geometrically implausible synthetically generated objects are avoided. Then, they are linearly interpolated to generate new models, which are arranged in the cube. This is done by following a logic based on their elongation and irregularity levels so that it is possible to extract trends from the errors of each method. It is important to remark that in nature there are a multitude of other shapes that are not included in the shape-cube and that, in this work, are considered as outliers. In the case of a body external to the shape space, an extrapolation would be required, not considered in this work. In this section the logic behind the construction of the shape-cube is described.

The Starting Cube Fifteen minor body models have been chosen as the bases of the shape space. Their selection is driven by the fact that they are well known minor bodies. This choice allows, in presence of an unknown body, to move around the space defined by these models to get an interpolated model whose shape is similar to the examined one. These initial shapes are the starting point to construct the

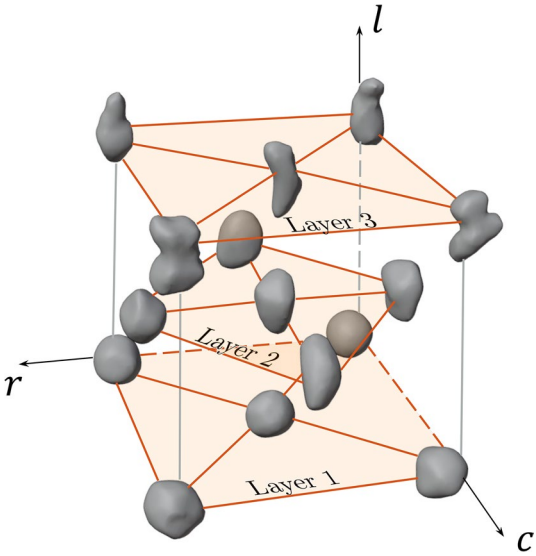

Fig. 3 Cube of known minor bodies' models. The first layer is made of near-spherical bodies that are Bennu, Pallas, Juno, Iris and Flora. The second layer consists of bodies that can be approximated to ellipsoids: Astrea, Lutetia, Gaspra, Ida and Parthenope. The third layer is made of elongated and irregular bodies, namely Eros, Toutatis, Mithra, Itokawa and comet 67P. Along the drawn lines intermediate models are generated

hyper-cube of shapes, made up of three layers, ordered from regular to irregular shapes:

1. The first layer is made of near-spherical bodies.
2. The second layer consists of bodies that can be approximated to ellipsoids.
3. The third layer is made of elongated and irregular bodies.

In order to identify the position of a body in the cube, three coordinates are required. For this reason the l, r, and c axes have been defined as follows. The three layers are stacked together such that the bodies elongation increases moving towards the positive l axis. Whereas, moving towards the positive r axis there is the transition from uniform to irregular bodies, while c is an ausiliar parameter that allows us to arrange the bodies in a three-dimensional structure achieving a better visualization. It must be noted that the bodies at the top of the cube are at the time being a limit case scenario for small-body elongation and irregularity, but more irregular objects could already exist or be discovered in the future leading to an update of the cube. An intuitive representation of the starting-cube is depicted in Fig. 3.

The Shape-Cube Since the starting cube models are the bases of the shape space, every element of the shape space may be written in a unique way as a finite linear combination of elements of the bases. Thus, synthetic intermediate models are generated as a linear interpolation of bases pair following the criterion described below for visualization purposes. Once the starting cube is constructed, the "Shape Keys" Blender[3] functionality has been exploited to merge the three-dimensional models. The software guarantees the preservation of the

[3] https://www.blender.org/, Last access: March 22, 2021.

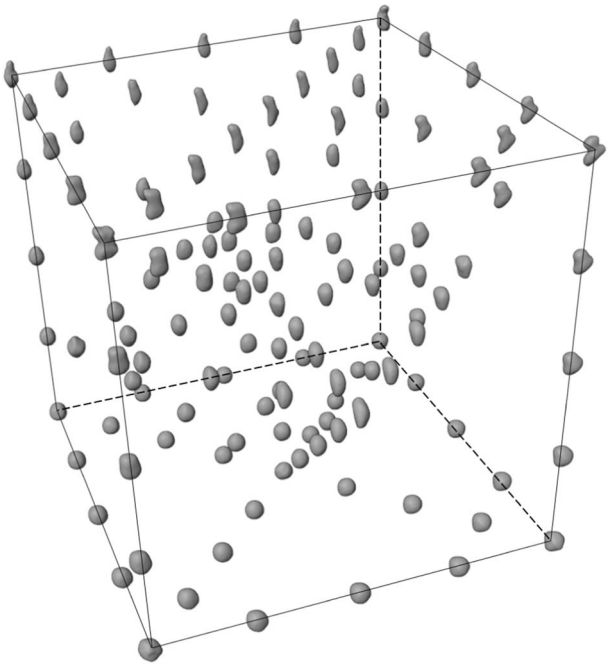

Fig. 4 Hyper-Cube of minor bodies' shapes. The drawn lines are the edges of the cube where the transition between two models happen

most important features of the starting models generating highly realistic minor bodies. A high number of intermediate models are generated starting from the known ones. The interpolation procedure in Blender consists of two steps: firstly, the mesh of the starting model is projected onto the shape of the final one, and secondly the corresponding vertices of the initial and projected models are linearly interpolated. This operator is indicated as $\oplus$, and it is realized as:

$$\mathcal{S}_w = w\mathcal{S}_1 \oplus (1-w)\mathcal{S}_2 \tag{6}$$

where $\mathcal{S}_1$ and $\mathcal{S}_2$ represent the set of mesh vertices of the initial and final bodies, $\mathcal{S}_w$ is the mesh of the interpolated model, while w is a weighting parameter. The set of weights used for the intermediate shapes are (0.25,0.5,0.75). Thus, for each pair of bodies, three additional intermediate shapes are generated. The importance of the intermediate models arises from the fact that it can be seen how the IP algorithms performances progressively shift from one shape to the other. The transitions were realized by following the cube edges and the internal lines drawn in Fig. 3. In addition, the models at the vertices of the second layer were fused with the central model of the first layer. The models at the vertices of the last layer were merged with the central body of the second one.

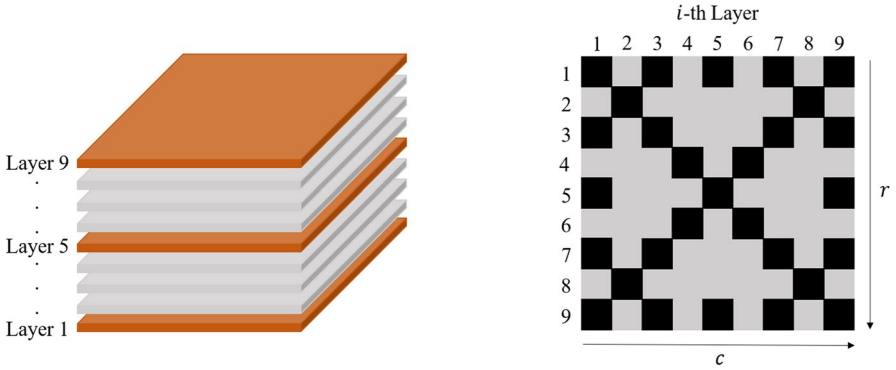

Fig. 5 Left: representation of the layers of the hyper-cube. Right: representation of one layer, where the squares indicate the presence of a model at that coordinate. Layers 1, 5 and 9 are highlighted as they are the ones with the shapes from the starting cube

The final hyper-cube of shapes, shown in Fig. 4, is made of 129 models and guarantees a large sample of small-body shapes to be investigated.

In order to identify the position of a small-body in the hyper-cube, each model coordinates are expressed as (l, r, c) triplets. These represent respectively the layer, the row and the column position in a defined layer. A graphical representation of the nine layers along with an example of the models arrangement in a generic layer, is depicted in Fig. 5.

2.3 Synthetic Image Generation

In order to test the image processing algorithms of different small-body shapes, it is important to have the capability to render a large set of images. These images are generated in Blender as it is an open source, simple to use rendering engine.[4] Blender's default reflectance model, named Principled BSDF (Bidirectional Scattering Distribution Function), is exploited to model the minor body surface reflectivity properties. A constant albedo value is also assumed. The typical characteristics of a CubeSat optical instrument are chosen. The camera, that generates gray-scale images, has a 1024×1024 pixels CCD (Charge–Coupled Device), 10 deg FOV, an 8-bit analog-to-digital converter and a 15% compression that reduces the image final size. Since the main focus of this work is related to shape robustness assessment, the following assumptions are made for the renderings:

– Ideal camera pointing: the camera points at the model center of mass. In this way it is possible to say that the location of the model CoM shall be projected to the image center.
– No blur: the target is completely in focus.

[4] https://www.blender.org/.

Fig. 6 Synthetic images of the model in position (9, 9, 5), that is the half-way point model of asteroids Toutatis and Mithra. **a** Image from the x point of view where the body seems to be spherical. In **b** and **c** there are model's images from the y and z axes perspective respectively

- No noise: the sensor and the environment are not generating noise in the images.
- No background: the background is completely dark so that there are no disturbances arising from stars or other celestial bodies.
- Known lighting conditions: the illumination vector acting on the small-body is assumed to be known on-board and all images are rendered with a 0 deg phase angle with respect to the Sun.

For better handling all models were scaled to the same overall size and it must be remarked that the performances are not affected by this choice. A sample image is depicted in Fig. 6.

Since from certain points of view, even a highly irregular body may look like a regular one, three distinct renderings are generated for each small-body shape by taking pictures from the three principal axes perspective: x, y and z. As a result the IP techniques were tested on 387 different synthetic images representing 129 different shapes.

From the x viewpoint all the models seem to be near-spherical that is a consequence of having the elongated side oriented as l axis, while from y and z, it is possible to appreciate their shape.

An example is given by the intermediate model of asteroid Mithra and Toutatis, in position (9, 9, 5) as can be seen in Fig. 6.

3 Results

In this section the four IP methods previously described are applied to all the hyper-cube models' images. As previously discussed, for each minor body, three different images are available. Their robustness is assessed and they are compared in order to understand what is the best method for a given small-body shape. It is necessary to introduce a metric to evaluate the methods robustness.

In this analysis, the error metric considered is the centroid position in the image, because not all the techniques considered produce range estimate to be compared. The estimated centroid is computed for each image, along with the Centroid Estimation Error [27] defined as:

$$\mathrm{CEE} = \sqrt{(x_{real} - x_c)^2 + (y_{real} - y_c)^2} \tag{7}$$

where (x_{real}, y_{real}) is the model CoM position, that is known to be in pixel (512, 512) thanks to ideal pointing conditions, and (x_c, y_c) is the estimated centroid. As a result, for each technique there are three hyper-cubes of errors, referred to as error-cubes. The errors are depicted as colored points and the higher the error the bigger the marker. For each technique the maximum and minimum color values are chosen considering 0 as lower bound and the global maximum error of the given technique as the upper bound. The complete tables with the numeric value of the CEE of each body is reported in the supplementary information. In the following, there will be a discussion on the performances of each technique based on the error-cube, then a global cube which assesses the best technique for a given shape is generated as a tool for mission design.

3.1 Center of Brightness

The center of brightness results are shown in Fig. 7, where it is possible to point out the CEEs by looking each body from the x, y, and z perspective. It is clear how the algorithm allows to obtain good results with every shape. Indeed, a maximum error of 31 pxl is achieved with asteroid Juno, that is in coordinates (1, 9, 9). This asteroid, shown in Fig. 8, is very peculiar as its shape appears to be intermediate between that of lumpy irregular bodies and near-spherical ones. From Fig. 7 it can be noted as the first layer (spherical minor bodies), a part from Juno, has very small errors in all three cubes. The error, as expected, increases on average by moving from the spherical objects to the irregular ones.

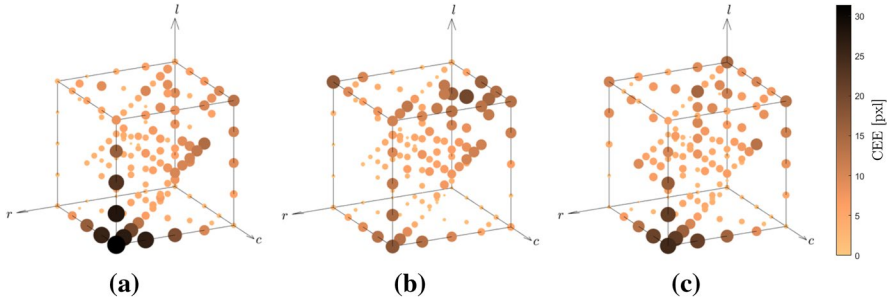

Fig. 7 Center of brightness method results. From **a** to **c** error-cube of the x,y and z axes is represented

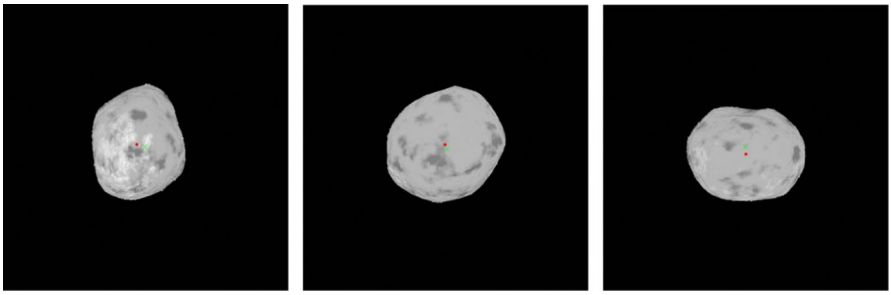

Fig. 8 Center of brightness algorithm applied to the asteroid at coordinates (1, 9, 9). The red dot is the estimated centroid while the green × is the real centroid position. From **a** to **c**; images taken from the *x*, *y* and *z* axis, respectively

3.2 Intensity Weighted Centroiding

In this section the results achieved with the IWC algorithm will be discussed. The resulting hyper-cubes of errors are depicted in Fig. 9.

The behaviour is similar to that of the center of brightness method, but with slightly higher errors. It can be noted that the maximum error is achieved with Juno and it is equal to 34.5 pxl as for the CoB method.

As for the center of brightness algorithm, good results are attained, indeed errors lower than 5 pxl are achieved.

It is questionable that if a minor body is not symmetrical, the centroid offset is large. An example is given by asteroid Eros, that is at coordinates (9, 5, 5). As shown in Fig.10, the asteroid is highly irregular but the method accurately finds the centroid position with an error close to zero. This finding, however, strongly depends on the rendering scene.

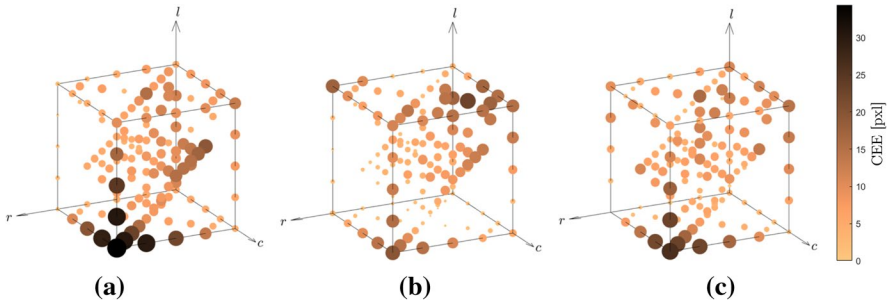

Fig. 9 Intensity weighted centroiding method results. From **a** to **c** error-cube of the *x*,*y* and *z* axes is represented

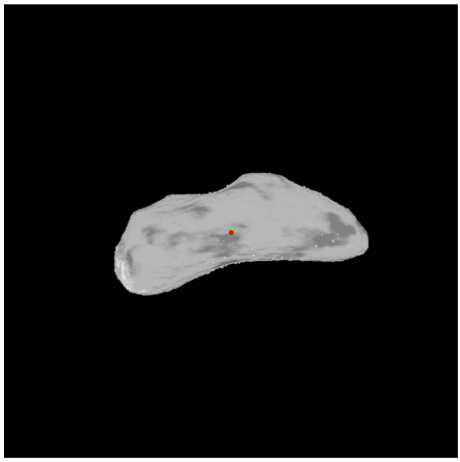

Fig. 10 Intensity weighted centroiding algorithm applied to the y perspective of the asteroid in position (9, 5, 5). The red dot is the estimated centroid while the green $\times$ is the real centroid position

3.3 Correlation with Lambertian Spheres

It is already known how the correlation with Lambertian spheres method performs well for bodies that can be approximated to a sphere. The resulting errors on the hyper-cube can be seen in Fig.11.

From the image it is clear that the robustness of this algorithm is very poor, and good results are reached just for near-spherical models. Indeed, when all the bodies seem to be spherical, from the x point of view, the algorithm returns excellent results, with the highest error given by asteroid Juno. However, from the y and z axes perspectives the targets are no more circular and the error progressively increases moving from the spherical models to the irregular ones. The maximum error is achieved with the irregular asteroid Eros and it is equal to 100 pxl.

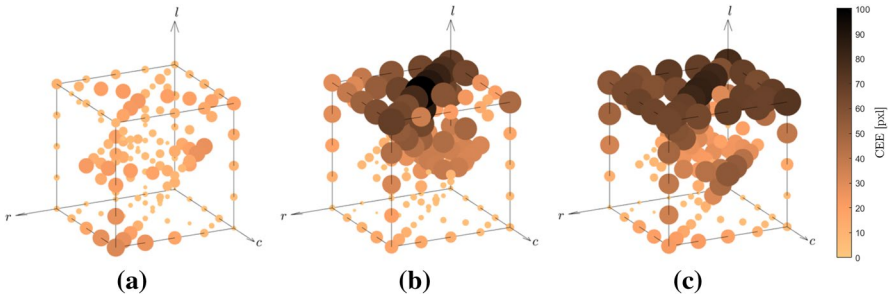

Fig. 11 Correlation with Lambertian spheres method results. From **a** to **c** error-cube of the x,y and z axes is represented

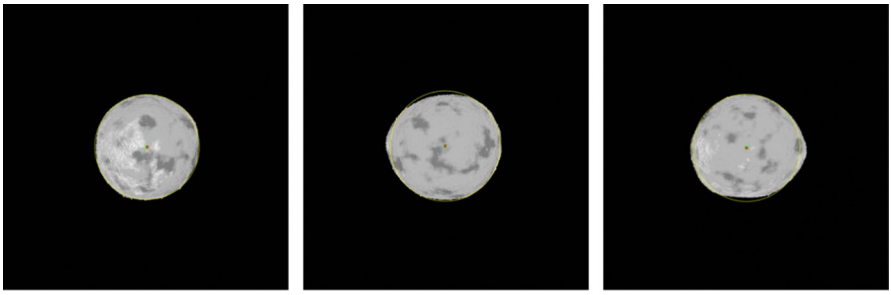

Fig. 12 Correlation with Lambertian spheres algorithm applied to the asteroid in position (1, 8, 2). The red dot is the estimated centroid while the green × is the real centroid position. From **a** to **c** images taken from the x, y and z axis, respectively

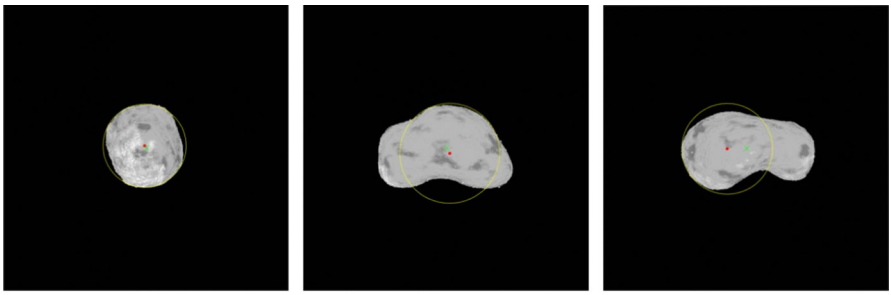

Fig. 13 Correlation with Lambertian spheres algorithm applied to the asteroid in position (9, 5, 9). The red dot is the estimated centroid while the green × is the real centroid position. From **a** to **c** images taken from the x, y and z axis, respectively

From the asteroids in the first layer, the high accuracy of the algorithm with near-spherical objects can be appreciated. For instance the errors associated to the asteroid in position (1, 8, 2) reach a maximum of 3 pxl as can be seen in Fig.12.

An example of an irregular minor body, is the model with coordinates (9, 5, 9). It is the intermediate model of comet 67P and asteroid Mithra. As depicted in Fig. 13, it is clear from the z point of view that the model is made of two lobes. This algorithm finds the maximum correlation in correspondence of the bigger lobe. Evidently the body is not well approximated. This demonstrate how the irregular shape bodies cannot be approximated to a sphere.

3.4 Ellipse Fitting

Lastly, the results obtained with the fitting algorithm are shown in Fig. 14.

The ellipse fitting method, results to be more flexible than the correlation one, in fact the maximum error achieved is about 30 pxl. As can be seen in Fig. 14, apart

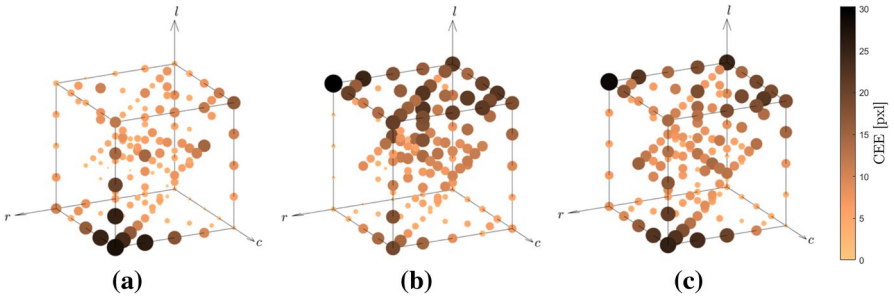

Fig. 14 Ellipse fitting method results. From **a** to **c** error-cube of the x,y and z axes is represented

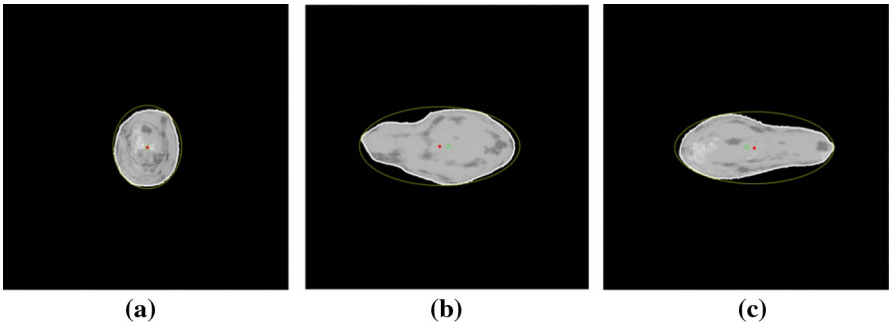

Fig. 15 Ellipse fitting algorithm applied to the asteroid in position (9, 9, 1). The red dot is the estimated centroid while the green × is the real centroid's position. From **a** to **c** images taken from the x, y and z axis, respectively

from Juno, the highest errors are in the irregular bodies' layer. In Fig.15 there are the results obtained with the elongated body Toutatis in position (9, 9, 1).

The model is characterized by a shape that is very different from that of an ellipsoid. However the fitting algorithm shows good performances obtaining errors up to 15 pxl in the z perspective.

3.5 Methods Comparison

After the performances of each method have been discussed separately, in this section the best performing methods are evaluated over the different shape models. Each method is characterized by three error-cubes, along the three axes. To make a comparison more realistic, it was decided to have just one error-cube per method. Since, one perspective is not more important than the others, a simple arithmetic mean of the error-cubes of each technique is made. Eventually, four error-cubes, one per method, are obtained.

To understand which is the method that best works on a given shape, the technique characterized by the minimum centroiding estimation error is chosen. The end results is what is called the final-cube, which highlight the expected best performing

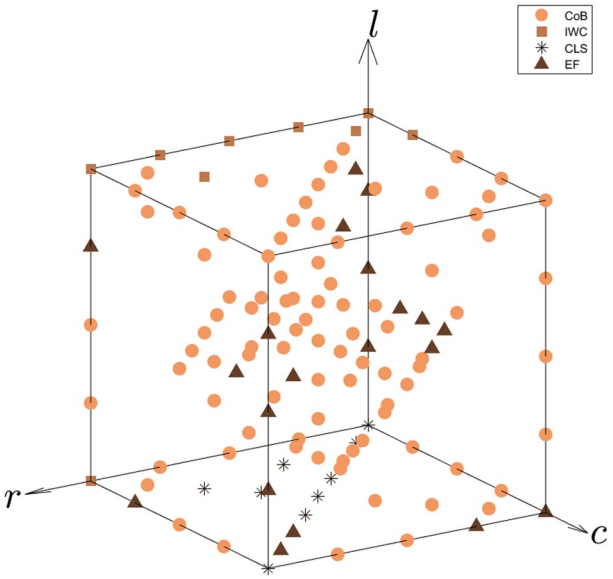

Fig. 16 The Final-Cube. Each marker represents the best technique for a given shape

method based on the shape seen from different view-points. For this cube it is possible to know what is the technique that best performs on a given body. The overall final-cube is depicted in Fig. 16, while in Fig. 17 the final-cube has been cut in slices so that each layer is individually reported. From the final-cube it is clear that the center of brightness method is the most versatile. It allows to get good results for every body type.

The intensity weighted centroiding accuracy is slightly worse than the center of brightness one. From Figs. 16 and 17 it can be noted that it returns the smallest errors for regular elongated bodies, like Toutatis and Itokawa. At the moment there is not a precise explanation for this result that could depend on the rendering scenes.

The correlation with Lambertian spheres method allows to obtain excellent results for near-spherical bodies, but very poor ones increasing the irregularity level of the target. This method is recommended when it is certain that the minor body can be approximated to a sphere.

Finally, the ellipse fitting method does not excel for a particular body type, but it seems to be the best choice for some specific shapes that span the shape-cube. Indeed it has a spread behaviour and it is more flexible with respect to the Lambertian spheres. The minima errors are achieved both for spherical and ellipsoidal bodies.

The results achieved were expected and reflect the weaknesses and strengths of the analyzed methods discussed in Sect. 2.1. The only peculiarity is given by the IWC technique previously discussed.

The wide amount of shapes is of vital importance as they help to investigate the trends of the analyzed methods shifting from one shape to the other. If only few

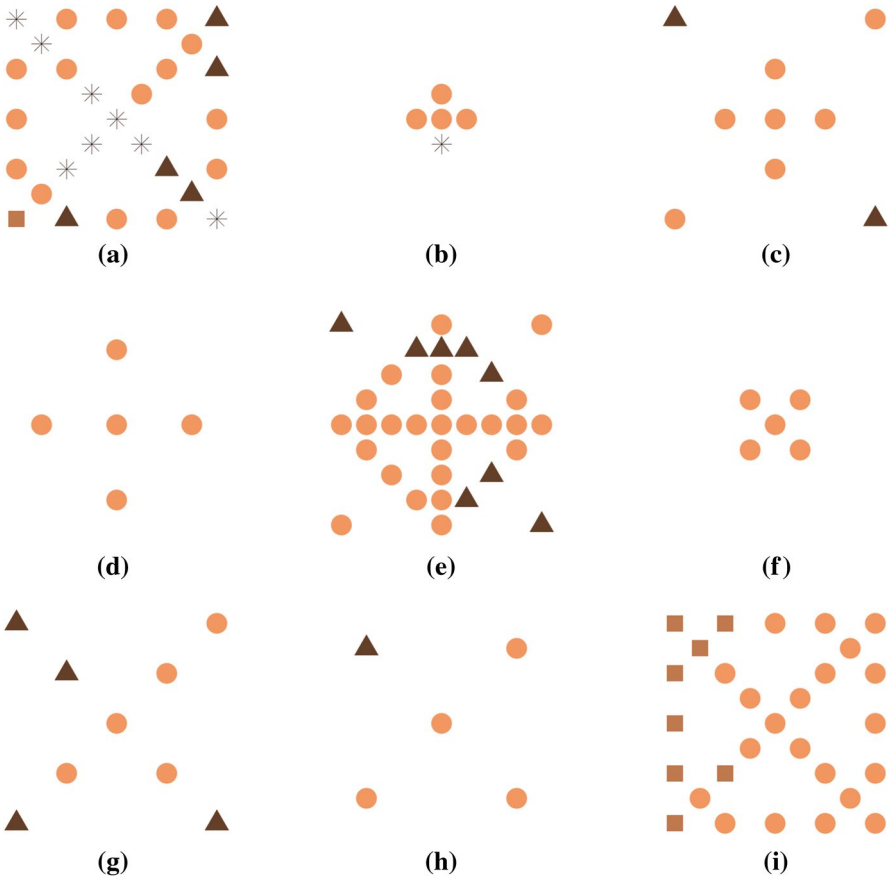

Fig. 17 Final-Cube cut in nine slices. From layer 1 (**a**) to layer 9 (**i**)

bodies were tested it would not be possible to extract patterns from the available data, and thus suggest the best performing algorithm for a given shape.

From the analysis of these results it is clear that if the body's shape to study is not priorly known, the CoB method is the best one, both for simplicity and accuracy. It can also be used as initial guessed method to navigate the body, and once information on the shape are available the spacecraft's on-board computer can autonomously select the best method to use.

4 Conclusions

Four traditional and well known image processing algorithms, namely center of brightness, intensity weighted centroiding, least square based ellipse fitting and correlation with Lambertian spheres are implemented in this work and tested over 129 artificially generated bodies arranged in a cubic structure based on their irregularity

and elongation. Synthetic images in the resolved regime and in a fully lighting condition, are realized to test the performance and robustness of the aforementioned techniques. The final-cube is constructed by taking for each body in the cube, the technique with the minimum average centroiding estimation error. Finally, there is the possibility to tell the mission designer what is the best performing method accordingly to the shape of the analyzed body. This selection map could also be integrated on-board the spacecraft so that it can autonomously select the best method after the shape is classified.

As a result, a shape space has been defined starting from fifteen well known minor bodies, considered as the bases of the space. They have been linearly interpolated in order to get the hyper-cube on which the IP methods are tested. It is important to highlight that the shapes considered in this work are not exhaustive at all. Indeed, extremely elongated and irregual bodies might exist, which are considered as outliers. The outcome is that the correlation with Lambertian spheres algorithm is the less versatile, but can achieve the best accuracy when the target body can be approximated to a sphere. The ellipse fitting method yields to get good results for spherical and ellipsoidal bodies, but it does not excel in any of the categories. The intensity weighted centroiding shows that it is the best method when there are elongated bodies without particular irregularities. Lastly, the center of brightness technique does provide good rough estimates that are computationally cheap, and it is the most versatile as small offsets are obtained for all body types.

Supplementary Information The online version contains supplementary material available at https://doi.org/10.1007/s40295-022-00348-6.

Acknowledgements M.P. and F.T. would like to acknowledge the funding received from the European Union's Horizon 2020 research and innovation programme under the Marie Skłodowska–Curie Grant Agreement No 813644.

Funding Open access funding provided by Politecnico di Milano within the CRUI-CARE Agreement.

Declarations

Conflict of interest The authors declare there are no conflict of interest.

References

1. Quadrelli, M., et al.: Guidance, navigation, and control technology assessment for future planetary science missions. J. Guid. Control Dyn. **38**, 1165–1186 (2015). https://doi.org/10.2514/1.G000525
2. Zacny K. et al.: Asteroid mining. In: Proceedings of the AIAA SPACE 2013 Conference and Exposition (2013)

3. Asphaug, E.: Growth and evolution of asteroids. Annu. Rev. Earth Planet. Sci. **37**, 413–448 (2009). https://doi.org/10.1146/ANNUREV.EARTH.36.031207.124214
4. Li, M., Huang, Y., Gong, S.: Assessing the risk of potentially hazardous asteroids through mean motion resonances analyses. Astrophys. Space Sci. **364**, 1–12 (2019). https://doi.org/10.1007/s10509-019-3557-5
5. Sugiura, K., Kobayashi, H., Inutsuka, S.: Toward understanding the origin of asteroid geometries-variety in shapes produced by equal-mass impacts. Astron. Astrophys. **620**, A167 (2018). https://doi.org/10.1051/0004-6361/201833227
6. Scheeres, D.: Orbital Motion in Strongly Perturbed Environments: Applications to Asteroid, Comet and Planetary Satellite Orbiters. Springer, New York (2012)
7. Takahashi, S., Scheeres, D.: Autonomous navigation and exploration of a small near-Earth asteroid (AAS 20-514). In: Proceedings of the AAS/AIAA Astrodynamics Specialist Conference (2020)
8. Wright, A., Liounis, A., Ashman, B.: Optical navigation algorithm performance. In: Proceedings of the 1st Annual RPI Workshop on Image-Based Modeling and Navigation for Space Applications (2018)
9. Franzese, V., Di Lizia, P., Topputo, F.: Autonomous optical navigation for the lunar meteoroid impacts observer. J. Guid. Control Dyn. **42**, 1579–1586 (2019). https://doi.org/10.2514/1.G003999
10. Christian, J.: Optical navigation using planet's centroid and apparent diameter in image. J. Guid. Control Dyn. **38**, 192–204 (2015). https://doi.org/10.2514/1.G000872
11. Christian, J., Robinson, S.: Noniterative horizon-based optical navigation by Cholesky factorization. J. Guid. Control Dyn. **39**, 1–9 (2016). https://doi.org/10.2514/1.G000539
12. Mortari, D., Zanetti, R., D'Souza, C.: Image processing of illuminated ellipsoid. J. Spacecr. Rocket. **53**, 448–456 (2016). https://doi.org/10.2514/1.A33342
13. Pugliatti, M., Topputo, F.: Navigation about irregular bodies through segmentation maps. In: Proceedings of the 31st AAS/AIAA Space Flight Mechanics Meeting (2021)
14. Furfaro, R., Law, A.: Relative optical navigation around small bodies via extreme learning machines. In: Proceedings of the AAS/AIAA Astrodynamics Specialist Conference, pp. 1959–1978 (2016)
15. Furfaro R. et al.: Deep learning for autonomous lunar landing. In: Proceedings of the 2018 AAS/AIAA Astrodynamics Specialist Conference (2018)
16. Pugliatti, M., Franzese, V., Topputo, F.: Data-driven image processing for onboard optical navigation around a binary asteroid. J. Spacecr. Rocket. **59**, 1–17 (2021). https://doi.org/10.2514/1.A35213
17. Gil-Fernandez, J., Ortega-Hernando, G.: Autonomous vision-based navigation for proximity operations around binary asteroids. CEAS Space J. **10**, 287–294 (2018). https://doi.org/10.1007/s12567-018-0197-5
18. Liounis, A.: Limb based optical navigation for irregular bodies. In: Proceedings of the 1st Annual RPI Workshop on Image-Based Modeling and Navigation for Space Applications (2018)
19. Pellacani, A., et al.: HERA vision based GNC and autonomy. In: Proceedings of the 8th European Conference for Aeronautics and Space Sciences (EUCASS) (2019)
20. Pellacani, A., et al.: Semi-autonomous attitude guidance using relative navigation based on line of sight measurements: aim scenario. Acta Astronautica **152**, 496–508 (2018). https://doi.org/10.1016/j.actaastro.2018.08.051
21. Christian, J.: A tutorial on horizon-based optical navigation and attitude determination with space imaging systems. IEEE Access **9**, 19819–19853 (2021). https://doi.org/10.1109/ACCESS.2021.3051914
22. Kanatani, K., Rangarajan, P.: Hyper least squares fitting of circles and ellipses. Comput. Stat. Data Anal. **55**, 2197–2208 (2011). https://doi.org/10.1016/j.csda.2010.12.012
23. Li, S., et al.: Image processing algorithms for deep-space autonomous optical navigation. J. Navig. **66**, 605–623 (2013). https://doi.org/10.1017/S0373463313000131
24. Bhaskaran, S., Riedel, J., Synnott, S.: Autonomous nucleus tracking for comet/asteroid encounters: the Stardust example. IEEE Aerosp. Conf. Proc. **97**, 353–365 (1998). https://doi.org/10.1109/AERO.1998.687921
25. Delabie, T., Schutter, J., Vandenbussche, B.: An accurate and efficient gaussian fit centroiding algorithm for star trackers. J. Astronaut. Sci. **61**, 1–25 (2015). https://doi.org/10.1007/s40295-015-0034-4
26. Benhacine, L.: Optical aberrations and their effect on the centroid location of unresolved objects. MA thesis. West Virginia University (2017)
27. Akondi, V., Roopashree, M., Prasad, B.: Improved iteratively weighted centroiding for accurate spot detection in laser guide star based Shack Hartmann sensor. Proc. SPIE **7588**, 45–54 (2010)
28. Muinonen, K., Lumme, K.: Disk-integrated brightness of a Lommel- Seeliger scattering ellipsoidal asteroid. Astron. Astrophys. **584**, A23 (2015). https://doi.org/10.1051/0004-6361/201526456

29. Kaasalainen, M., Tanga, P.: Photocentre offset in ultraprecise astrometry: implications for barycentre determination and asteroid modelling. Astron. Astrophys. **416**, 367–373 (2004). https://doi.org/10.1051/0004-6361:20031711
30. Pugliatti, M., Topputo, F.: Small-body shape recognition with convolutional neural network and comparison with explicit features based method. In: Proceedings of the 2020 AAS/AIAA Astrodynamics Specialist Conference (2020)
31. Topputo F. et al.: Lunar meteoroid impact observer: a CubeSat at Earth- Moon L2. In: Proceedings of the 42nd COSPAR Scientific Assembly (2018)
32. Fitzgibbon, A., Pilu, M., Fisher, R.: Direct Least-Squares fitting of ellipses. IEEE Trans. Pattern Anal. Mach. Intell. **21**, 253–257 (1996). https://doi.org/10.1109/34.765658